Journal of Computational Physics 386 (2019) 248–263

Contents lists available at ScienceDirect

Journal of Computational Physics

www.elsevier.com/locate/jcp

Efficient simulation of thermally fluctuating biopolymers immersed in fluids on 1-micron, 1-second scales

Kai Liu [a], John Lowengrub [a,b,c], Jun Allard [a,b,d,*]

[a] Department of Mathematics, University of California at Irvine, United States of America
[b] Center for Complex Biological Systems, University of California at Irvine, United States of America
[c] Department of Biomedical Engineering, University of California at Irvine, United States of America
[d] Department of Physics, University of California at Irvine, United States of America

ARTICLE INFO

Article history:
Received 22 August 2017
Received in revised form 15 December 2018
Accepted 20 December 2018
Available online 22 February 2019

Keywords:
Stochasticity
Thermal fluctuation
Stokes flow
Fluid-structure interaction
Actin
Filament

ABSTRACT

The combination of fluid-structure interactions with stochasticity, due to thermal fluctuations, remains a challenging problem in computational fluid dynamics. We develop an efficient scheme based on the stochastic immersed boundary method, Stokeslets, and multiple timestepping. We test our method for spherical particles and filaments under purely thermal and deterministic forces and find good agreement with theoretical predictions for Brownian Motion of a particle and equilibrium thermal undulations of a semi-flexible filament. As an initial application, we simulate bio-filaments with the properties of F-actin. We specifically study the average time for two nearby parallel filaments to bundle together. Interestingly, we find a two-fold acceleration in this time between simulations that account for long-range hydrodynamics compared to those that do not, suggesting that our method will reveal significant hydrodynamic effects in biological phenomena.

1. Introduction

Since cells are composed largely of water, cell biology fundamentally involves fluid-structure interactions. Indeed, fluid dynamics is a key driver of many cell biological phenomena, including the swimming of both eukaryotes and bacteria, ciliary beating [1], and cell blebbing [2,3]. More surprisingly, recent research is demonstrating that fluid dynamics is also an important player in organelle positioning in large cells like oocytes [4,5], some surface crawling of both eukaryotes [6] and bacteria [7], ultra-fast endocytosis in neurons [8], and transient cell-cell contact by immune cells [9].

To understand these flows, computational biologists have developed tools such as the Immersed Boundary Method (IBM) [10] and used these to simulate cellular phenomena [8,11,12]. All of the above-listed cellular phenomena play out over seconds timescales and involve entire cells or regions of cells, thereby necessitate micron-length-scale modeling.

On the other hand, cellular matter falls into the class of *soft* matter, meaning that thermal fluctuations can dominate its behavior. Thermal fluctuations have been demonstrated to drive many cellular processes [13,14]. Few studies have included both thermal fluctuations and fluid-structure interaction, even though there is evidence that some cellular phenomena involve both [9].

Previous work to do so has been led by Atzberger [15–19] and others [20,21] including us [22]. These methods involve solving the Landau-Lifshitz Navier–Stokes equation (see Eqs. (5)–(8) below), or its low-Reynolds analogue. A significant

* Corresponding author.
E-mail address: jun.allard@uci.edu (J. Allard).

https://doi.org/10.1016/j.jcp.2018.12.039
0021-9991/

finding of previous research, which we highlight in this work, is that thermal fluctuations implicate the inertial timescale $\tau_{\text{inertia}} =\sim 10^{-12}$ s (which depends on the required spatial scale of interest). This is counter-intuitive, since the length- and time-scales of interest suggest we are safely in the low-Reynolds regime. As a consequence, straightforward numerical simulations are limited to numerical timesteps $\Delta t \sim \tau_{\text{inertia}}$, and cannot practically be used to simulate cell biological phenomena, which often play out over seconds.

In this work, we present a scheme for simulating fluid-structure interactions with thermal fluctuations over long timescales. Our method is capable of simulating structures with soft material properties of biological matter: biopolymers with the flexural rigidity of the cytoskeleton and membranes with the bending coefficient of the cell's plasma membrane. Importantly, we perform simulations of a 1-micron cube box up to 1 second. This takes approximately 1 week of computing time, opening up practical cell-biological application.

Several computational techniques combine to allow us this efficiency, which we mention here and discuss in depth in Section 4. First, we extend previous work [16] by solving for the flow averaged over a short time, i.e., instead of solving for the instantaneous flow field $\mathbf{v}(x, y, z, t)$, we solve for with the flow averaged over a short time interval Δt at constant position,

$$\mathbf{u}(x, y, z, t) = \frac{1}{\Delta t} \int_{t}^{t+\Delta t} \mathbf{v}(x, y, z, t')\, dt'. \tag{1}$$

Second, we employ two nested timesteps, with thermal fluctuations only acting on the outer timestep. We show below that the dynamics on the inner time step are sufficiently smooth to allow a third computational technique: an implicit solver based on Broyden's method [30]. Fourth, we split the linear flow into two parts, one solved using IBM and the other by a regularized Stokeslet method, allowing spatial discretization much larger than would be possible with IBM alone. Finally, we parallelize the algorithm using a GPU implementation.

As a specific application, we apply our method to compute the bundling of actin filaments, molecules that are key players in many cell biological processes [23]. By including hydrodynamic interactions, we improve upon previous simulations to understand actin bundling [14]. We find that hydrodynamic interactions accelerates bundling by a factor of two, for physiological parameters, and that this acceleration can be partly understood in terms of a nonzero covariance between pairs of filaments.

The paper is organized as follows. In Section 2, we introduce the physical model using the IBM framework. In Section 3, we discretize the system in preparation for numerical evaluation. In Section 4, we develop a numerical method based on a steady Stokes formulation. We accelerate the numerical simulation by first combining the Stokeslets Method with the Stochastic Immersed Boundary method (SIBM) and, second, by developing an implicit, multiple-timestep method. We test our numerical scheme in Section 5. And, finally, we apply our method to bundling biopolymers in Section 6. We end with a discussion of limitations and future applications in Section 7.

2. Model statement

Consider a bio-structure immersed in a fluid, parameterized by coordinate $\mathbf{X}$. In general, this could be a bio-membrane such as the cell membrane, but here we restrict our attention to bio-filaments, such as microfilaments made of the protein actin. These linear polymers are semi-flexible (meaning they are typically shorter than their persistence length) and relatively strong, resisting buckling by multi-piconewton compressive forces and filament fracture by nanonewton tensile forces.

To understand the dynamics of such filaments immersed in fluid, the width of the filament is important: A thick filament must displace more fluid when it moves laterally compared to a thin filament, therefore thick filaments fluctuate slower than thin filaments. Specifying the width of a filament in a numerical scheme presents a difficulty since the straightforward way to capture these molecular details is to use a finer grid, significantly increasing the computational cost of the problem. We return to this issue in Section 4.2.

For a filament, we use the standard elastic energy

$$\Phi(\mathbf{X}) = \int_{L} \left(\frac{B}{2} H^2 + \lambda \right) dl \tag{2}$$

where B is the bending rigidity, where l parametrizes the one-dimensional space curve describing the centerline of the filament,

$$H = \left\| \frac{d^2 X}{dl^2} \right\| \tag{3}$$

is the mean curvature and λ is a Lagrange multiplier to enforce conservation of the length of the filament, specifically

$$\left\| \frac{dX}{dl} \right\| = 1. \tag{4}$$

Table 1
Model parameters. Note the parameter R will appear in Eq. (44).

Symbol	Meaning	Value	Reference
ρ	Mass density of fluid and structure	10^3 kg/m^3	(value for water)
η	Viscosity of fluid	1.0 m Pa s	(value for water)
k_BT	Thermal energy unit	4.1×10^{-21} J	(value at 20 °C)
B	Bending rigidity of F-actin filament	4.2×10^{-26} Nm^2	[14]
R	Radius of F-actin filament	2.5×10^{-9} m	[14]
L	Length of F-actin filament	100–300 nm	[14]

Then $\mathbf{F_X} = -\nabla_{\mathbf{X}}\Phi(\mathbf{X})$ is the elastic force density associated with configuration $\mathbf{X}$.

For a 3D fluid domain $\mathcal{D}$ containing viscous fluid with viscosity η and density ρ, parameterized by Eulerian coordinate $\mathbf{x}$, containing an immersed structure $\mathbf{X}$, the equations of motion are [15–17,21,24],

$$\rho\frac{\partial \mathbf{v}}{\partial t} = \eta\nabla^2\mathbf{v} - \nabla p + \mathbf{f} + \mathbf{f}_{thm}, \tag{5}$$

$$\nabla\cdot\mathbf{v} = 0, \tag{6}$$

$$\frac{d\mathbf{X}}{dt} = \gamma[\mathbf{v}]. \tag{7}$$

Eqs. (5) and (6) describe dynamics of the fluid. Here $\mathbf{v}$ is the velocity, p is the pressure, and $\mathbf{f}$ represents the influence of the immersed structure. In the stochastic immersed boundary formulation,

$$\mathbf{f} = \Gamma[\mathbf{F_X}] + \nabla_{\mathbf{X}}\Gamma k_BT \tag{8}$$

where Γ is a (smoothed) delta function describes how a structure influences the nearby fluid, and the term $\nabla_{\mathbf{X}}\Gamma k_BT$ arises from the thermal fluctuations associated with the momentum of the structure, which disappears by a zero mass assumption of the structure [16,17]. We note that this term is a gradient of a scalar function and it changes only the pressure but not the velocity field in an incompressible fluid. Thermal fluctuations are contained in $\mathbf{f}_{thm}$, which satisfies

$$\langle \mathbf{f}_{thm}(\mathbf{x},s)\mathbf{f}^T_{thm}(\mathbf{y},t)\rangle = -2k_BT\eta\nabla^2\delta(\mathbf{x}-\mathbf{y})\delta(t-s). \tag{9}$$

Eq. (7) is the equation of motion of the immersed structure, e.g., the filaments. The linear operator γ describes how the structure moves with the fluid, and Γ and γ are adjoint operators [16,17]. We make use of a standard choice for these operators [10,15,16], described in Eq. (32). Using these operators to describe a filament of specified radius, R, in 3 dimensions raises difficulties that we discuss in Sec. 4.2.

Typical parameters we use in this work are shown in Table 1.

3. Spatial and temporal discretization in the Stokes limits

In this section, we discretize Eq. (5) in preparation for numerical implementation. We describe three regimes in which the timescale of interest could fall, one of which (iii) is the Stokes limit. We do this with the help of an average velocity defined over a time period Δt,

$$\mathbf{u}^n \equiv \frac{1}{\Delta t}\int_{t^n}^{t^{n+1}} \mathbf{v}(s)ds, \tag{10}$$

where $\mathbf{v}(t)$ is the instantaneous velocity at time t. In the Stokes regime, this allows us to choose a discretization that reduces the computational cost significantly.

The Eulerian fluid domain $\{\mathbf{x}|\mathbf{x}\in\Omega\}$ is resolved by a finite difference discretization. The fluid variables (velocity field $\mathbf{v}$ and pressure field p) are represented on a periodic grid with length L along each direction, M grid points along each direction, and grid spacing $\Delta x = L/M$. The discrete version of Eqs. (5) and (6) is given by

$$\rho\frac{d\mathbf{v_m}}{dt} = \eta\mathcal{L}\mathbf{v_m} - Dp_{\mathbf{m}} + \mathbf{f_m} + \mathbf{f}_{thm}(\mathbf{x_m},t), \tag{11}$$

$$\nabla\cdot\mathbf{v_m} = 0. \tag{12}$$

Here $\mathcal{L}$ is the 7 point discrete Laplacian, D is the central difference gradient, $\mathbf{f_m}$ is from the immersed structure by the fluid-structure coupling, and $\mathbf{v_m}$ is the instantaneous velocity. Note that thermal fluctuations in the system are derived through the kinetic energy of the fluid, so the mass appears as a linear prefactor and cannot be simply set to zero to reduce to Stokes' equations [16]. The discrete Fourier transform of the fluid variables yields

$$\hat{\mathbf{v}}_{\mathbf{k}} = \frac{1}{N^3}\sum_{\mathbf{m}} \mathbf{v}_{\mathbf{m}} e^{-2\pi i \mathbf{k}\cdot\mathbf{m}/M}, \tag{13}$$

$$\mathbf{v}_{\mathbf{m}} = \sum_{\mathbf{k}} \hat{\mathbf{v}}_{\mathbf{k}} e^{2\pi i \mathbf{k}\cdot\mathbf{m}/N}. \tag{14}$$

Here each sum is over the N^3 lattice points defined by $\mathbf{m} = \{m_1, m_2, m_3\}$ and $\mathbf{k} = \{k_1, k_2, k_3\}$, where $0 \le m_i \le M-1$ and $0 \le k_i \le M-1$ for $i = 1, 2, 3$.

Eqs. (11) and (12) in Fourier space read as

$$\frac{d\hat{\mathbf{v}}_{\mathbf{k}}}{dt} = -\alpha_{\mathbf{k}}\hat{\mathbf{v}}_{\mathbf{k}} - i\rho^{-1}\hat{p}_{\mathbf{k}}\mathbf{g}_{\mathbf{k}} + \rho^{-1}\hat{\mathbf{f}}_{\mathbf{k}} + \rho^{-1}\hat{\mathbf{f}}_{thm,\mathbf{k}}, \tag{15}$$

$$\mathbf{g}_{\mathbf{k}} \cdot \hat{\mathbf{v}}_{\mathbf{k}} = 0, \tag{16}$$

where

$$\alpha_{\mathbf{k}} = \frac{2\eta}{\rho\Delta x^2}\sum_{l=1}^{3}\left[1 - \cos\left(2\pi \mathbf{k}^{(l)}/M\right)\right], \tag{17}$$

$$\mathbf{g}_{\mathbf{k}} = \sin\left(2\pi \mathbf{k}^{(l)}/M\right)/\Delta x. \tag{18}$$

The thermal fluctuations in Fourier space are [15,16]

$$\hat{\mathbf{f}}_{thm,\mathbf{k}} = \rho\sqrt{2D_{\mathbf{k}}}\,\frac{d\tilde{\mathbf{B}}_{\mathbf{k}}(t)}{dt}. \tag{19}$$

The $D_{\mathbf{k}}$ denotes the strength of thermal fluctuations in the $\mathbf{k}$-th mode,

$$D_{\mathbf{k}} = \begin{cases} \frac{k_B T}{2\rho L^3}\alpha_{\mathbf{k}}, & \text{for } \mathbf{k} \in \mathcal{H}, \\ \frac{k_B T}{\rho L^3}\alpha_{\mathbf{k}}, & \text{for } \mathbf{k} \notin \mathcal{H}, \end{cases} \tag{20}$$

where $\mathcal{H} = \{\mathbf{k} | k_i = 0, M/2, i = 1, 2, 3\}$. Stochasticity is introduced by $\tilde{\mathbf{B}}_{\mathbf{k}}(t)$, which denotes a complex-valued Brownian motion process with the real and imaginary parts of each Cartesian component consisting of an independent standard Brownian motion process (which is dimensionless).

Using Itô's calculus, the instantaneous velocity in Fourier space is computed from Eq. (15) to give

$$\hat{\mathbf{v}}_{\mathbf{k}}(t^{n+1}) = \hat{\mathbf{v}}_{\mathbf{k}}(t^n)e^{-\alpha_{\mathbf{k}}\Delta t} + \frac{1 - e^{-\alpha_{\mathbf{k}}\Delta t}}{\rho\alpha_{\mathbf{k}}}\xi_{\mathbf{k}}\hat{\mathbf{f}}^n_{\mathbf{k}} + \sqrt{2D_{\mathbf{k}}}\xi_{\mathbf{k}}\int_{t^n}^{t^{n+1}} e^{-\alpha_{\mathbf{k}}(t^{n+1}-s)}d\tilde{B}_{\mathbf{k}}(s), \tag{21}$$

where $\xi_{\mathbf{k}} = I - \mathbf{g}_{\mathbf{k}} \cdot \mathbf{g}^T_{\mathbf{k}}/|\mathbf{g}_{\mathbf{k}}|^2$ is the projection orthogonal to $\mathbf{g}_{\mathbf{k}}$. The average velocity $\mathbf{u}_{\mathbf{m}}$ over a time period Δt is

$$\mathbf{u}_{\mathbf{m}}(t) = \frac{1}{\Delta t}\sum_{\mathbf{k}}\int_{t^n}^{t^{n+1}}\left(e^{-\alpha_{\mathbf{k}}(s-t)}\hat{\mathbf{v}}_{\mathbf{k}}(t) + \frac{1 - e^{-\alpha_{\mathbf{k}}(s-t)}}{\rho\alpha_{\mathbf{k}}}\xi_{\mathbf{k}}\hat{\mathbf{f}}^n_{\mathbf{k}} + \sqrt{2D_{\mathbf{k}}}\xi_{\mathbf{k}}\int_t^s e^{-\alpha_{\mathbf{k}}(s-u)}d\tilde{B}_{\mathbf{k}}(u)\right)\cdot e^{2\pi\mathbf{k}\cdot\mathbf{m}/N}ds. \tag{22}$$

Using the definition of the Itô integral [25], the double integral can be written as

$$\int_{t^n}^{t^{n+1}}\int_t^s e^{-\alpha_{\mathbf{k}}(s-u)}dB(u)ds = \frac{1}{-\alpha_{\mathbf{k}}}\int_{t^n}^{t^{n+1}} e^{-\alpha_{\mathbf{k}}(t+\Delta t-u)}dB(u) + \frac{B(t+\Delta t) - B(t)}{\alpha_{\mathbf{k}}}, \tag{23}$$

giving the average velocity in Fourier space,

$$\begin{aligned}\hat{\mathbf{u}}^n_{\mathbf{k}} = &\left(\frac{1 - e^{-\alpha_{\mathbf{k}}\Delta t}}{\alpha_{\mathbf{k}}\Delta t}\right)\hat{\mathbf{v}}^n_{\mathbf{k}} + \left(\frac{\alpha_{\mathbf{k}}\Delta t - (1 - e^{-\alpha_{\mathbf{k}}\Delta t})}{\alpha^2_{\mathbf{k}}\Delta t}\right)\rho^{-1}\xi_{\mathbf{k}}\hat{\mathbf{f}}^n_{\mathbf{k}} \\ &- \frac{\sqrt{2D_{\mathbf{k}}}}{\alpha_{\mathbf{k}}\Delta t}\int_{t^n}^{t^{n+1}} e^{-\alpha_{\mathbf{k}}(t+\Delta t-s)}\xi_{\mathbf{k}}d\mathbf{B}_{\mathbf{k}}(s) + \frac{\sqrt{2D_{\mathbf{k}}}}{\alpha_k\Delta t}\left(\xi_{\mathbf{k}}\mathbf{B}_{\mathbf{k}}(t^{n+1}) - \xi_{\mathbf{k}}\mathbf{B}_{\mathbf{k}}(t^n)\right)\end{aligned} \tag{24}$$

The above is valid for any choice of timestep Δt. However, we observe that several natural timescales emerge from the dynamics, leading to three categories [16]:

i. $\Delta t \ll \min \frac{1}{\alpha_k}$, when the time step is sufficiently small that the dynamics of all modes of the fluid are resolved by the stochastic immersed boundary method.

ii. $\min \frac{1}{\alpha_k} \lesssim \Delta t \lesssim \max \frac{1}{\alpha_k}$, when the fluid dynamics are only partially resolved.

iii. $\max \frac{1}{\alpha_k} \ll \Delta t \ll \tau_{mov}(a)$, when the time step is large enough to underresolve all modes of the fluid, but small enough to resolve the dynamics of the immersed structure. Here $\tau_{mov}(a)$ denotes the time required for an elementary particle to move a displacement equal to the grid size either by advection or diffusion. We refer to this as the Stokes regime.

For our system of interest, $\Delta x = 5 \times 10^{-9}$ m, $\eta = 10^{-3}$ Pa s and $\rho = 10^3$ kg/m^3, $\min \frac{1}{\alpha_k} \approx \frac{2\rho \Delta x^2}{9\eta} \approx 10^{-12}$ s and $\max \frac{1}{\alpha_k} \approx 10^{-8}$ s. This gives $\Delta t \gg \max \frac{1}{\alpha_{\mathbf{k}}} = 10^{-8}$ s, suggesting we are in the Stokes motion regime. We also confirm that $\tau_{mov}(a)$ is sufficiently large, *a posteriori*: We run a simulation up to 2×10^3 steps using SIBM with $\Delta t = 5 \times 10^{-7} s$. The average value of the displacement for each point on the filament over Δt is $0.0324 \Delta x$, with a standard deviation $0.031 \Delta x$, which means $\Delta t = 5 \times 10^{-7}$s $\ll \tau_{\mathrm{mov}}$(a). We therefore seek an expression of Eq. (24) in this limit.

To derive this, we exploit the fact that in Brownian motion, subsequent increments of motion are independent. This implies $\hat{\mathbf{v}}_{\mathbf{k}}^n$ is independent of $\int_{t^n}^{t^{n+1}} e^{-\alpha_{\mathbf{k}}(t-s)} \xi_{\mathbf{k}} d\mathbf{B}_{\mathbf{k}}(s)$ and $\left(\xi_{\mathbf{k}} \mathbf{B}_{\mathbf{k}}(t^{n+1}) - \xi_{\mathbf{k}} \mathbf{B}_{\mathbf{k}}(t^n)\right)$. On the other hand, $\int_{t^n}^{t^{n+1}} e^{-\alpha_{\mathbf{k}}(t-s)} \xi_{\mathbf{k}} d\mathbf{B}_{\mathbf{k}}(s)$ and $\left(\xi_{\mathbf{k}} \mathbf{B}_{\mathbf{k}}(t^{n+1}) - \xi_{\mathbf{k}} \mathbf{B}_{\mathbf{k}}(t^n)\right)$ are not independent. The variance of the stochastic terms reads as

$$\mathbb{E}\left[-\frac{\sqrt{2D_{\mathbf{k}}}}{\alpha_k \Delta t} \mathrm{Re}\left(\int_{t^n}^{t^{n+1}} \mathrm{e}^{-\alpha_k(t-s)} \mathrm{d}\mathbf{B}_{\mathbf{k}}(s) \right) + \frac{\sqrt{2D_{\mathbf{k}}}}{\alpha_k \Delta t} \mathrm{Re}\left(\mathbf{B}_{\mathbf{k}}(t^{n+1}) - \mathbf{B}_{\mathbf{k}}(t^n) \right) \right]^2$$
$$= \frac{2D_{\mathbf{k}}}{(\alpha_k \Delta t)^2} \left(\frac{2\alpha_{\mathbf{k}} \Delta t - 3 - e^{-2\alpha_{\mathbf{k}} \Delta t} + 4e^{-\alpha_{\mathbf{k}} \Delta t}}{2\alpha_{\mathbf{k}}} \right), \tag{25}$$

given $\mathbb{E}\left[\mathrm{Re}\left(\int_{t^n}^{t^{n+1}} e^{-\alpha_{\mathbf{k}}(t^{n+1}-s)} d\mathbf{B}_{\mathbf{k}}(s) \right) \mathrm{Re}\left(\mathbf{B}_{\mathbf{k}}(t^{n+1}) - \mathbf{B}_{\mathbf{k}}(t^n) \right) \right] = \frac{1}{\alpha_{\mathbf{k}}}(1 - e^{-\alpha_{\mathbf{k}} \Delta t})$. Since $1 \ll \alpha_{\mathbf{k}} \Delta t$ and $e^{-\alpha_{\mathbf{k}} \Delta t} \ll 1$ in the Brownian motion regime, Eq. (24) reduces to

$$\hat{\mathbf{u}}_{\mathbf{k}}^n = (\alpha_{\mathbf{k}} \rho)^{-1} \xi_{\mathbf{k}} \hat{\mathbf{f}}_{\mathbf{k}}^n + \frac{\sqrt{2D_{\mathbf{k}}}}{\alpha_k \Delta t} \sqrt{\Delta t - \frac{3}{2\alpha_{\mathbf{k}}}} \xi_{\mathbf{k}} \hat{\Xi}_{\mathbf{k}}, \tag{26}$$

where $\Xi_{\mathbf{k}}$ is a complex normal random variable. This average velocity can be interpreted as the solution of the below system of equations as a Stokes limit of Eqs. (5), (6), (7) and (9),

$$\eta \nabla^2 \mathbf{u} - \nabla p + \mathbf{f} + \bar{\mathbf{f}}_{thm}(t) = 0, \tag{27}$$
$$\nabla \cdot \mathbf{u} = 0, \tag{28}$$
$$\frac{d\mathbf{X}}{dt} = \gamma[\mathbf{u}], \tag{29}$$
$$\bar{\hat{\mathbf{f}}}_{thm,\mathbf{k}}(t) = \frac{\rho \sqrt{2D_{\mathbf{k}}}}{C_{\mathbf{k}}(\Delta t)} \hat{\Xi}_{\mathbf{k}}, \tag{30}$$

where $C_{\mathbf{k}}(\Delta t) = \sqrt{\frac{2\alpha_{\mathbf{k}} \Delta t^2}{2\alpha_{\mathbf{k}} \Delta t - 3}} > 1$. Heuristically, we can think of $C_{\mathbf{k}}(\Delta t)$ as a "cooling" factor that reduces the amplitude of thermal fluctuations. This factor arises in the above analysis because, without it, it is not possible to satisfy both the Brownian motion relation in the time interval Δt and the kinetic energy $m_{unit} \mathbf{u}^2/2 = 3k_B T/2$ (where m_{unit} is the mass of fluid in a unit cube of fluid).

4. Numerical implementation

The immersed boundary formulation in Eqs. (27)–(30) could be used to simulate stochastic dynamics of the system. However, it is challenging to accurately specify the size of the immersed structure — in our case, the size of molecules that make up the filaments — since the fluid-structure coupling "smooths" the boundary of the spherical molecules. Especially when the size of the structure is small, e.g. a spherical particle of radius 2.0–2.5 nm, the grid size of the fluid needs to be much smaller than the filament to approximately resolve the size of the particle, which is computationally inefficient. To overcome this, in this section, we introduce a linear decomposition of the Stokes equation. In this decomposition, the velocity of the fluid induced by the filament is computed by the regularized Stokelets method, which naturally discerns the size of particles in the domain, while the coupling with the structure is solved using the immersed boundary framework.

4.1. Interpolation for the immersed boundary method

The interpolation of the velocity for the structure is implemented by a smoothing function. At timestep n,

$$\gamma[\mathbf{u}^n] = \sum_{\mathbf{m}} \mathbf{u}^n_{\mathbf{m}} \delta_a \left(\mathbf{x}_m - \mathbf{X}^n\right) a^3, \tag{31}$$

where the sum is over the index m which indexes the (Eulerian) spatial discretization of the fluid. The smoothing function δ_a is defined as [10,15,16]

$$\delta_a(\mathbf{x}) = \frac{1}{a^3}\varphi\left(\frac{|x|}{a}\right)\varphi\left(\frac{|y|}{a}\right)\varphi\left(\frac{|z|}{a}\right) \qquad \text{for} \quad \mathbf{x} = (x, y, z), \tag{32}$$

where a is parameter related to the support of δ_a, and

$$\varphi(r) = \begin{cases} \frac{1}{8}(3 - 2r + \sqrt{1 + 4r - 4r^2}) & \text{for } 0 \le r \le 1, \\ \frac{1}{8}(5 - 2r - \sqrt{-7 + 12r - 4r^2}) & \text{for } 1 < r \le 2, \\ 0 & \text{for } 2 < r. \end{cases} \tag{33}$$

4.2. Describing the structure using a Stokeslets method

As we discussed before, for a filament immersed in the fluid, the molecular width of the filament is important. However, specifying the width of a filament in immersed boundary method presents a difficulty. One needs to use finer grid and a spherical mesh with grid size $\Delta x \ll r$, where r is the radius of a spherical ball, in order to clearly characterize the shape of the ball. To avoid this, we split the total average velocity into two parts,

$$\mathbf{u} = \mathbf{u}_1 + \mathbf{u}_2, \tag{34}$$

where

$$\eta\nabla^2\mathbf{u}_1 - \nabla p_1 - \bar{\mathbf{f}}_{thm}(t) = 0, \tag{35}$$

$$\nabla \cdot \mathbf{u}_1 = 0, \tag{36}$$

that resolves the thermal fluctuation, and

$$\eta\nabla^2\mathbf{u}_2 - \nabla p_2 + \mathbf{f} = 0, \tag{37}$$

$$\nabla \cdot \mathbf{u}_2 = 0, \tag{38}$$

that resolves the presence and influence of the structure, i.e., the bio-filaments. Only Eqs. (37)–(38) will be solved using the Stokeslet framework, while Eqs. (35)–(36) will be solved using the immersed boundary framework as described above.

We represent the filament by a string of balls. To do this, we turn to the regularized Stokeslets method, which naturally resolves the size of a spherical structure to describe proteins making up the filament. In the regularized Stokeslets method, a force density is described by

$$\eta\nabla^2\mathbf{u}_2 - \nabla p_2 + \mathbf{f} = 0 \tag{39}$$

$$\nabla \cdot \mathbf{u}_2 = 0, \tag{40}$$

$$\mathbf{f} = \mathbf{F}_{\mathbf{X}_j}\phi_\varepsilon(\mathbf{x} - \mathbf{X}_j), \tag{41}$$

where ϕ_ε is a radically symmetric cutoff function with the property that $\int \phi_\varepsilon(\mathbf{x})d\mathbf{x} = 1$ and ε is a parameter that controls the spreading.

Note that operator Γ to spread the Lagrange force in the immersed boundary method is replaced by the cutoff function ϕ_ϵ, which can also be thought of as a smoothed δ function. Moreover, no interpolation is needed to calculate the velocity of the balls on the filament since $\mathbf{u}_2$ simply locates on the Lagrange frame $\mathbf{X}$ at the center of each protein molecule. Also note that unlike the periodic boundary conditions imposed for the flow field $\mathbf{u}_1$ in a cube of size L^3, here we assume an infinite domain for $\mathbf{u}_2$ (as is natural for Stokeslets methods). For a fluid domain much larger than $4l_o \le L$, where l_o is the total length of a filament, the influence of the periodic boundary condition onto the filament is small, especially for $\mathbf{u}_1$ induced by thermal fluctuation, that the linear combination of the two is valid.

In the regularized Stokeslets method, the velocity of a spherical particle in the fluid domain is [26,27]

$$u_i(\mathbf{X}_q) = \frac{1}{8\pi\eta}\sum_{s=1}^{N_s}\sum_{j=1}^{3}\omega_s F_{\mathbf{X}_s,j} S^\varepsilon_{ij}\left(\mathbf{X}_q, \mathbf{X}_s\right), \tag{42}$$

for $i = 1, 2, 3$, where N_s is the total number of beads comprising the structure, $\mathbf{F}_{\mathbf{X}_s} = \left(F_{\mathbf{X}_s,1}, F_{\mathbf{X}_s,2}, F_{\mathbf{X}_s,3}\right)$ is the elastic force on the s-th bead for $q, s = 1, 2, ..., N_s$, $\{\omega_1, \omega_2, \omega_3, ..., \omega_{N_s}\}$ are the quadrature weights, and

$$S_{ij}^{\varepsilon}\left(\mathbf{X}_s, \mathbf{X}_q\right) = \frac{\delta_{ij}(r^2 + 2\varepsilon^2) + r_i r_j}{(r^2 + \varepsilon^2)^{3/2}}, \tag{43}$$

for $i, j = 1, 2, 3$, is the regularized Stokeslets. In Eq. (43), we use the notation $\mathbf{r} = \{r_1, r_2, r_3\} = \mathbf{X}_s - \mathbf{X}_q$, and $r = \|\mathbf{r}\|_2$.

To compute ε we use the Stokes drag relation for a spherical ball,

$$\mathbf{F} = 6\pi\eta R\mathbf{v}, \tag{44}$$

where $\mathbf{v}$ is the velocity of a ball with radius R immersed in a fluid of viscosity η and dragged by a force $\mathbf{F}$. We assume $\omega_0 = 1$, $N_s = 1$ and $r = 0$ in Eqs. (42) and (43) [27,28] and get $\varepsilon = 3\Delta x/4$ for a single particle. The actin filament is modeled as a string of spherical balls of the same size connected without overlapping. This choice allows the symmetry of a spherical ball to agree with the radical symmetry of the cutoff function ϕ_ε. To further confirm that this approximation is appropriate, we also performed purely immersed boundary simulations in which we simulated a string of spherical balls where each ball is composed of 3 layers of points, with nearby points connected by rigid springs to preserve shape, finding reasonable agreement (within 95% for each point).

4.3. Elastic force acting on the filament

The discretized bending energy from Eq. (2) is given by

$$E_b = \sum_{i=1}^{N_s-1} \frac{1}{2} B H_i^2 \Delta L_i, \tag{45}$$

where $\Delta L_i = \left(L_{\mathbf{X}_{i-1}\mathbf{X}_i} + L_{\mathbf{X}_i\mathbf{X}_{i+1}}\right)/2$ and $L_{\mathbf{X}_{i-1}\mathbf{X}_i} = \|\mathbf{X}_i - \mathbf{X}_{i-1}\|^2$ is the length from $\mathbf{X}_{i-1}$ to $\mathbf{X}_i$. The curvature is approximated by

$$H_i = \frac{\varphi_i}{\Delta L_i}, \tag{46}$$

where φ_i is the small angle between vectors $\mathbf{X}_i - \mathbf{X}_{i-1}$ and $\mathbf{X}_{i+1} - \mathbf{X}_i$. Thus the bending energy at the ith bead is

$$E_i = \frac{1}{2}\frac{\varphi_i^2}{\Delta L_i}. \tag{47}$$

Taking the variational derivative, the bending force working on the ith bead $\mathbf{F}_i^{[i]}$ induced by E_i is

$$\mathbf{F}_i^{[i]} = -2B\frac{H_i}{\Delta L_i}\mathbf{n}_i, \tag{48}$$

where $\mathbf{n}_i$ is perpendicular to $\overline{\mathbf{X}_{i-1}\mathbf{X}_{i+1}}$. Note that here we consider half the total bending energy since $\mathbf{F}_i^{[i]}/2 = -\mathbf{F}_i^{[i+1]} = -\mathbf{F}_i^{[i-1]}$, which are all induced by E_i. Also note that, in the variational approach, we measure the small displacement of the ith node $\mathbf{X}_i$ with respect to the mass center of the two segments $\overline{\mathbf{X}_{i-1}\mathbf{X}_i}$ and $\overline{\mathbf{X}_i\mathbf{X}_{i+1}}$ in the Lagrange framework. Therefore, net force and net torque are zero, and the total bending force on the ith bead is

$$\mathbf{F}_{i,B} = \mathbf{F}_i^{[i]} - \frac{1}{2}(\mathbf{F}_{i-1}^{[i]} + \mathbf{F}_{i+1}^{[i]}), \quad \text{for } i = 1, 2, ..., N-1. \tag{49}$$

We assume neighboring nodes on the filaments are connected by elastic springs with spring potential

$$E_L = \sum\nolimits_{i=1}^{N_s} \frac{\lambda_L}{2}(L_{\mathbf{X}_{i-1}\mathbf{X}_i} - \Delta L)^2, \tag{50}$$

where λ_L is the spring constant, and $\Delta L = L/N_s$ is the equilibrium arclength. The tension between two neighboring nodes then reads as

$$\mathbf{F}_{[i],L} = \lambda_L\left(L_{\mathbf{X}_{i-1}\mathbf{X}_i} - \Delta L\right)\frac{\mathbf{X}_{i+1} - \mathbf{X}_i}{\|\mathbf{X}_{i+1} - \mathbf{X}_i\|}, \tag{51}$$

for $i = 0, 1, 2, \cdots, N_s - 1$, acting on the ith node and pointing to the $(i+1)$ node. Finally the total force acting on the ith node is given by

$$\mathbf{F}_{\mathbf{X}_i}(t) = \mathbf{F}_{[i],L} - \mathbf{F}_{[i-1],L} + \mathbf{F}_{i,B}, \quad \text{for } i = 1, 2, ..., N-1. \tag{52}$$

For the two open ends of a filament, analogous versions of Eq. (49) and (52) are derived in a similar manner.

Table 2
Computational cost comparison.

Method	SIBM inertia	Brownian explicit	Brownian implicit
Inner timestep size	10^{-12} s	10^{-11} s	10^{-8} s
Time cost for 1 s	100 years (est.)	10 years (est.)	10 days

4.4. Implicit scheme and multiple timesteps

Bending rigidities introduce a severe timestep restriction that scales as $\Delta t \propto \Delta x^4$ for explicit methods [32,33]. To overcome this, we take advantage of the fact that the stochastic immersed boundary method is computationally expensive while the Stokeslets method is cheap, and introduce a multiple timestep approach. First, we define an inner timestep Δt_{inner} that is smaller than the outer timestep Δt by an integer factor (we typically use $\Delta t = 100\Delta t_{\text{inner}}$ or $\Delta t = 1000\Delta t_{\text{inner}}$). The SIBM update of $\mathbf{u}_1$ is performed once per outer timestep. Secondly, during each Δt_{inner} we use the Stokeslets method to evolve the structure immersed in the fluid, assuming that during each single period Δt, the thermal noise is not changed.

This allows us to use a relatively small inner timestep. However, we find that this is still insufficient to obtain numerical stability at our desired computational expense. Because the bending rigidity for the filaments is stiff, e.g. $B = 4.2 \times 10^{-26}$ J for a typical actin filament, explicit methods will not converge for timestep larger than 10^{-11} s. Therefore, in the inner timestep, we make use of an implicit time discretization coupled with the Broyden method [30] for solving nonlinear equations at each inner timestep. This method is an approximation of the Newton method to solve an implicit equation, except instead of solving the Jacobian Matrix in each iteration, we use the Sherman-Morrison formula to update directly (and approximately) the inverse of the Jacobian matrix [31].

The Broyden Method is given as follows. We first use the secant method to construct the Jacobian matrix of the elastic force $\mathbf{J_F}$ numerically. The shape of the filament is updated by

$$\mathbf{X}^{n+1} = \mathbf{X}^n + \delta\mathbf{X}, \tag{53}$$

where

$$\delta\mathbf{X} = \Delta t \left[\mathcal{L}^{-1}\left(\mathbf{F}[\mathbf{X}^{n+1}]\right) + \gamma[\mathbf{u}_1]\right], \tag{54}$$

and $\mathcal{L}$ is the linear operator describing the Stokeslets method. We set

$$\mathbf{G}(\mathbf{X}) = \mathbf{X} - \mathbf{X}^n - \Delta t \left[\mathcal{L}^{-1}\left(\mathbf{F}[\mathbf{X}]\right) + \gamma[\mathbf{u}_1]\right] = 0, \tag{55}$$

to be the nonlinear system. In the Newton method, the update involves solving

$$\mathbf{J}\delta\mathbf{X} = -\mathbf{G}(\mathbf{X}^n) \tag{56}$$

where

$$\mathbf{J} = \mathbf{I} - \Delta t\mathcal{L}^{-1}\mathbf{J_F}. \tag{57}$$

In the Broyden method, we instead use the current estimate of the Jacobian matrix $\mathbf{J}_{n-1}$ and improve it by taking the solution to the secant equation that is a minimal modification to $\mathbf{J}_{n-1}$ [30,31]:

$$\mathbf{J}_n = \mathbf{J}_{n-1} + \frac{\Delta\mathbf{G}_n - \mathbf{J}_{n-1}\Delta\mathbf{x}_n}{\|\Delta\mathbf{x}_n\|^2}\Delta\mathbf{x}_n^{\mathrm{T}}. \tag{58}$$

The computation times are shown in Table 2. We find the explicit method is stable for $\Delta t_{\text{inner}} < 10^{-11}$ s, while the implicit method is stable at $\Delta t_{\text{inner}} \geq 10^{-7}$ s. We find the computational cost is cheaper for the implicit method, even though it requires us to solve a nonlinear system each inner timestep.

For implicit schemes, there is a tradeoff in terms of computational expense between small timesteps, which require fewer Broyden iterations but more steps, and larger timesteps, which may require more Broyden iterations but fewer steps. For given outer timestep Δt, in order to have the highest computational efficiency, we performed a series of tests to study the different timestep choices. Within each Δt, we use the Broyden method to evolve the semi-deterministic system by step size Δt_{inner}. The performance of different choice of Δt_{inner} is given in Table 3. For our parameters, we find that $\Delta t_{\text{inner}} = 2 \times 10^{-8}$, $\Delta t = 5 \times 10^{-7} s$ is the most efficient choice.

5. Numerical tests

In this section, we test our numerical scheme against a battery of scenarios in which the solution is known, exactly or approximately. Taken together, the tests in this section demonstrate good agreement for scenarios with particles and extended bodies; time dynamics and equilibrium; with and without thermal fluctuations.

Table 3
Average Iteration Numbers (times in seconds).

Δt_{inner}	10^{-9}	10^{-8}	2×10^{-8}	5×10^{-8}	10^{-7}
Iterations per Δt_{inner}	6.2	9.4	16	32	107
Iterations per Δt (outer)	3127	467	392	318	535
Stability	Stable	Stable	Stable	Unstable	Unstable

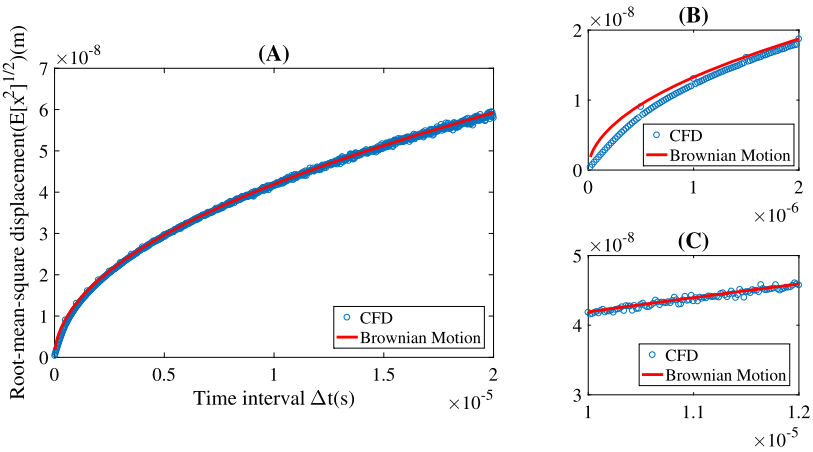

Fig. 1. Tracing the dynamics of a sphere (a single point) diffusing in the fluid. Here Brownian motion relation is given as $\Delta x(\Delta t) \sim N(0, 2D\Delta t)$, where δt denotes the time period. (For interpretation of the colors in the figure(s), the reader is referred to the web version of this article.)

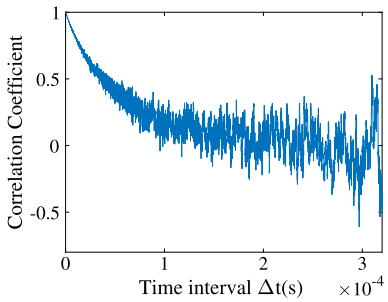

Fig. 2. The time dependence structure, $\text{cov}(y_R(s), y_R(s+t))$. Here we set the length of each filament is $L = 300$ nm. The filament is clamped at one end and free to move on the other side.

5.1. Dynamics of a diffusing particle

We apply our scheme to simulate a small particle immersed in the fluid subject to thermal fluctuations. Here we set $\Delta x = 5$ nm, the diameter of the particle is $R = \Delta x/2 = 2.5$ nm. The system is evolved using timesteps $\Delta t_{\text{inner}} = 2 \times 10^{-8}$ s and $\Delta t = 5 \times 10^{-7}$ s.

In Fig. 1, we report the mean displacement $|\Delta x|$ over time intervals δt. For longer times, we expect that this quantity obeys the relation

$$\Delta x(\delta t) \sim N(0, 2D\delta t). \tag{59}$$

This is indeed the case for times $\sim 10^{-5}$ s (A, C). As expected, there is disagreement for short times $\delta t \sim 10^{-6}$, where the relation (59) is not supposed to hold.

5.2. Thermal equilibrium of a free filament and limitation of the implicit method

In this test, a fluctuating filament is clamped on the left hand side and free to move at the other side. Suppose the filament lies along the positive x-axis. We set the length of the filament $L = 300$ nm, partitioned into 61 spherical beads. Under thermal fluctuations, it will have its unclamped tip experience a displacement given by the random variable P_R. We show the time autocorrelation of the tip displacement in Fig. 2, and its equilibrium distribution in Fig. 3A.

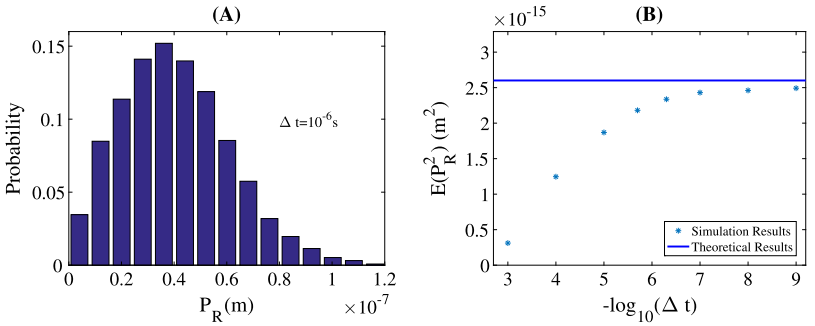

Fig. 3. [A] The probability distribution of P_R. [B] The $\mathbb{E}\left[P_R^2\right]$ as a function of Δt. For the fluctuating filaments that we are interested in, $\Delta t \leq 10^{-6}$ s is required.

We compute analytically the variance of P_R in thermal equilibrium, so we may compare it with our numerical results. We make two approximations to simplify calculations. First, we assume the lowest mode of deformation is dominant. Second, we approximate this mode's shape as having constant curvature H, i.e., an arc of a circle. This defines a geometry in which

$$P_R = \frac{1}{H}\left(1 - \cos(1 - P_R H)\right) \approx L^2 H, \tag{60}$$

giving this mode an energy

$$E = \frac{B P_R^2}{2L^3}. \tag{61}$$

This depends quadratically on P_R. Therefore, by the Equipartition Theorem, thermal equilibrium provides it with mean energy $\mathbb{E}[E] = \frac{1}{2}k_B T$, leading to

$$\mathbb{E}\left[P_R^2\right] = \frac{k_B T L^3}{B} \approx 2.6 \times 10^{-16}\ \mathrm{m}^2. \tag{62}$$

In Fig. 3B, we plot the mean of $\mathbb{E}\left[P_R^2\right]$ as a function of the outer timestep Δt. We find that there is a limit to the implicit method: For $\Delta t < 10^{-6}$ s, we find good agreement with the theoretical value from Eq. (62) (blue curve). For $\Delta t > 10^{-6}$ s, we find that our method deviates from the theoretical value. Heuristically, our method omits higher modes of fluctuations, so we interpret this timestep limit as the timescale below which the higher modes become significant compared to the lower modes in determining filament configuration. We elaborate on this in the following section.

5.2.1. Estimating the timestep limitations

Although our accelerated method correctly solves for the dynamics of a spherical particle immersed in the fluid, for a more complicated structure, the above results demonstrate a threshold for the time step size in the implicit method. We seek to provide a scaling estimate of this threshold. For a filament clamped at one end, the first mode of deflection is described by the equation (see [14] and previous subsection)

$$dy \approx -\left(\frac{B}{\eta L_C^4}\right) y\,\Delta t + \sigma\, d\tilde{B}_t, \tag{63}$$

where y denotes the displacement of the free end with respect to the equilibrium position, B is the bending rigidity, L_C is the contour length, and η is the viscosity. This SDE is of the form of the Ornstein-Uhlenbeck [35] stochastic differential equation,

$$y' = -\lambda y + dB_t/dt, \tag{64}$$

where $y(0) = 0$, for $0 \leq t \leq \infty$, and dB_t/dt is Gaussian white noise. It has been shown that the implicit Euler method,

$$y_{i+1} = \frac{1}{1+\lambda\Delta t} y_i + \frac{1}{1+\lambda\Delta t} dB_t^i, \tag{65}$$

leads to an underestimate of the variance of y unless $\lambda\Delta t \ll 1$ [35,36], that manifests itself as an over-damping effect.

For an explicit Euler method, the timestep limit is a strong threshold for stability that must be satisfied by every mode in our simulation. Therefore, the stability is required for the smallest element, $\Delta x \sim 5 \times 10^{-9}$. For our parameters, this sets a restriction for the timestep about $\Delta t < 1/\lambda \approx 10^{-11}$ s. For the implicit Euler method, the timestep criterion is a

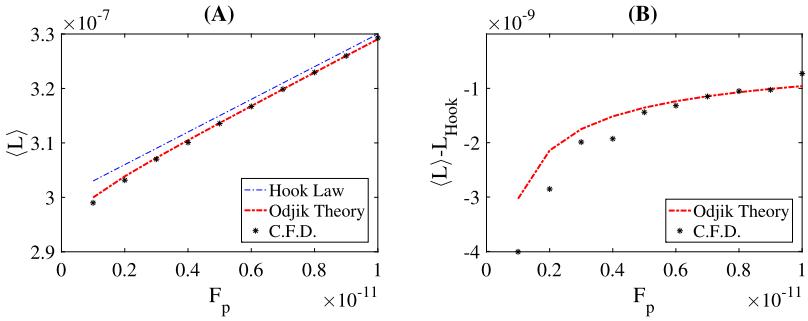

Fig. 4. Here the total length of the filament to be 0.3 μm, denoted by 61 connected beads, i.g. $\Delta x = 5$ nm, the bending stiffness 4.2×10^{-26} J. $\Delta t_{inner} = 2 \times 10^{-8}$ s, $\Delta t = 5 \times 10^{-7}$ s. [A] Simulation results compared to analytical theory from [29] in Eq. (66). [B] Nonlinear part of extension, $\langle L \rangle - L_{Hook} = -L_0 k_B T/(2\sqrt{BF_p})$, where $L_{Hook} = L_0 + F_p N_s/\lambda_L$.

rough scaling criterion for accuracy. Since configuration of the filament is dominated by its largest modes, and we want accuracy for the full filament length, $L = 3 \times 10^{-7}$. For the first two modes, $L_C \geq 1.5 \times 10^{-7}$. For our parameters, this leads to $\Delta t \leq 10^{-5}$ s before over-damping by our implicit scheme becomes dominant. This is in reasonable agreement with the onset of discrepancy we find in Fig. 3. Beyond this timestep, our method results in an underestimate of the variance of the filament's tip deflection, as expected for implicit schemes.

5.3. Thermal equilibrium of an entropic spring

A further test is provided by applying a constant force F_p to the end of the filament, directed along its axis [29]. Previously, Odjik $\Delta t = 5 \times 10^{-7}$ s pointed out that there is an approximate formula for the force-extension relation valid at high forces,

$$\mathbb{E}[L] = L_0 + F_p N_s/\lambda_L - L_0 k_B T/(2\sqrt{BF_p}). \tag{66}$$

Here L_0 is the original length of the filament with no tension or fluctuation, N_s is the number of the springs that connect the nodes on the filament, and F_p is the tension applied at the ends of the filament. Note that the above equation is valid only when $L_0 k_B T/\sqrt{BF_p} \ll F_p N_s/\lambda_L$ [29]. Thermal fluctuations, i.e., entropy, create an effective spring that resists pulling (first term), in addition to the Hookean force (second term).

As shown in Fig. 4, our simulations results agree with Eq. (66) for large forces. Here we set the total length of the filament to be 0.3 μm, denoted by 61 connected beads, i.e. $\Delta x = 5$ nm, that the diameter for each protein molecular is 2.5 nm. The bending stiffness 4.2×10^{-26} J, the timestep $\Delta t = 5 \times 10^{-7}$ s, and the inner timestep $\Delta t_{inner} = 2 \times 10^{-8}$ s. For clarity, in Fig. 4B, we plot only the nonlinear part of the displacement, corresponding to the last term in Eq. (66).

6. Application to the bundling of actin filaments

As an initial application of our scheme, we simulate the bundling of F-actin filaments. As mentioned above, actin is an abundant polymer that is responsible for many cellular processes. Individual actin filaments are relatively flexible, but many of the structures they form in cells comprise actin filaments that are bundled together. These structures include stress fibers, filopodia, and the cytokinetic ring [23]. Interestingly, filaments are not grown in bundles, therefore pre-existing filaments must find partners in order to form these structures. This interaction is mediated by bundling molecules like α-actinin and filamin [23,34], which are globular proteins a few nanometers in size. To explore this bundling processes, we simulate two filaments clamped at one end and separated by a distance $d = 100$ nm.

To compute a lower-bound on the time to bundling, we find the first time that the filaments are within 5 nm from each other, the approximate size of a bundling molecule. This corresponds to a distance between their centerlines of 10 nm. Note that, in the following, we refer to this lower bound as the bundling event, even though in reality a molecular reaction involving the bundling molecule will increase the bundling time. Our work follows an earlier study of actin bundling [14] that omitted hydrodynamic interactions between the filaments.

Since we are only interested in the time until the filaments are within 5 nm of each other (10 nm distance between centerlines), we stop the simulation the moment this condition is met. This obviates the need for us to deal with explicit steric (excluded volume) interaction forces, or inaccuracies due to two filament nodes being within the same Eulerian grid point.

6.1. Two fluctuating filaments: time series and bundling statistics

We set the total length of each filament to be 0.3 μm and use 61 connected beads, giving $\Delta x = 5$ nm. The base distance between the two bundling filaments is 100 nm. We set the timesteps to be $\Delta t_{\text{inner}} = 2 \times 10^{-8}$ s and $\Delta t = 5 \times 10^{-7}$ s. We

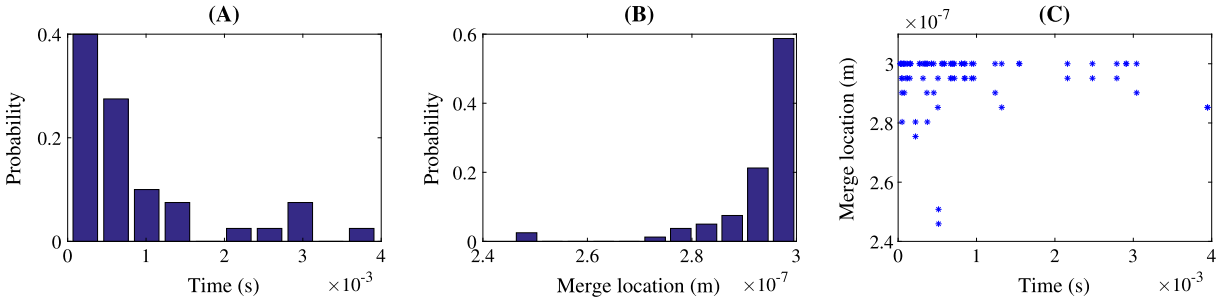

Fig. 5. The length of each filament is $L = 300$ nm. The distance between the two bundling filament is 100 nm. [A] Histogram of the bundling time. In these simulations, the two filaments share the same fluid. [B] Histogram of the bundling position. The average bundling position is at the right tip of the filament for both cases. [C] Bundling position vs bundling time.

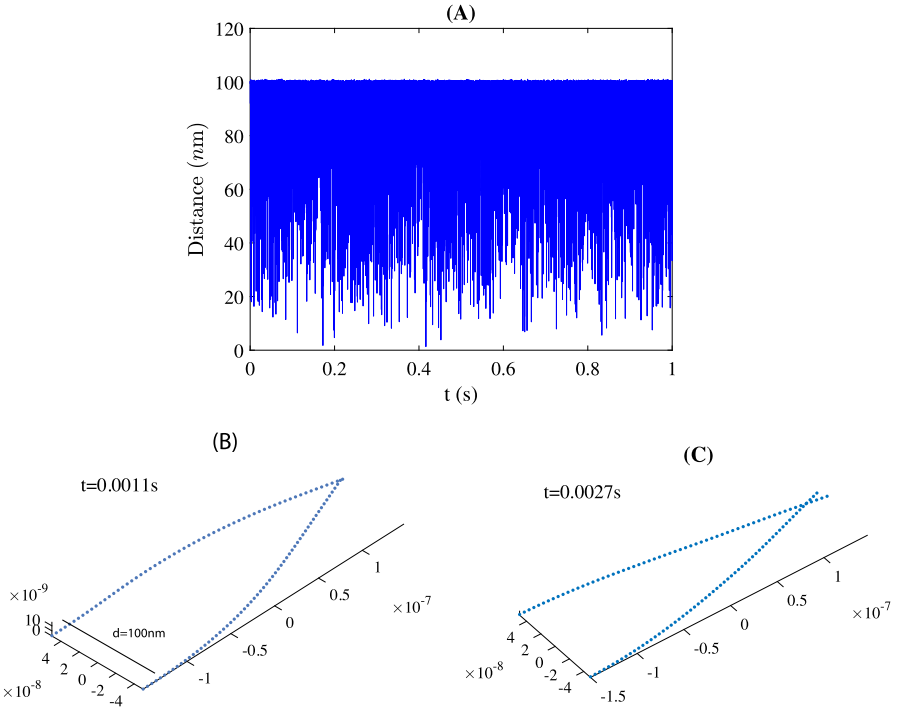

Fig. 6. The dynamics of bundling filaments up to one second. [A] The distance of the 2 filaments over 1 second. [B, C] Shape of the 2 filaments at the time of bundling proximity. Note that in both cases, the filament centerlines are separated by 10 nm, even though the perspective suggests they are in contact.

initialize the filaments in their unbent equilibrium positions and allow the simulation to run until a bundling event, which, as noted above, we define as any portion of the filaments reaching within 10 nm of each other. The distribution of bundling times is shown in Fig. 5A, where we plot the histogram of the bundling time for 30 simulations. The mean bundling time is 0.86×10^{-3} s. In Fig. 5 [B], we show the distribution of bundling positions, which is strongly biased towards tips of the filaments, as expected.

We also performed simulations up to 1 second, in which we do not stop the simulation upon bundling. In Fig. 6 we show the distance between the two filaments over 1 second (A), and two of the snapshots when the two filaments are in bundling proximity (B, C). In this time series, the two filaments bundle 6 times (where we consider multiple bundling events separated by less than 0.001 s as a single event).

Many previous simulations of stochastic motion of biostructures [14,34,37] omit direct simulation of the fluid, and therefore neglect hydrodynamic interactions between the immersed bodies. To understand the influence of hydrodynamics, we perform a hydrodynamic-free simulation as follows. We run two simulations with single filaments, recording the positions of these filaments at each time. We then perform a "virtual" bundling simulation in which these two simulations are replayed simultaneously, and look for the first bundling event, defined as above. We find the mean bundling time in this "no-fluid" case is $T_{\mathrm{nf}} = 1.1 \times 10^{-3}$ s. This is longer than for bundling simulations that include hydrodynamics, by a factor of 1.3 at this separation distance.

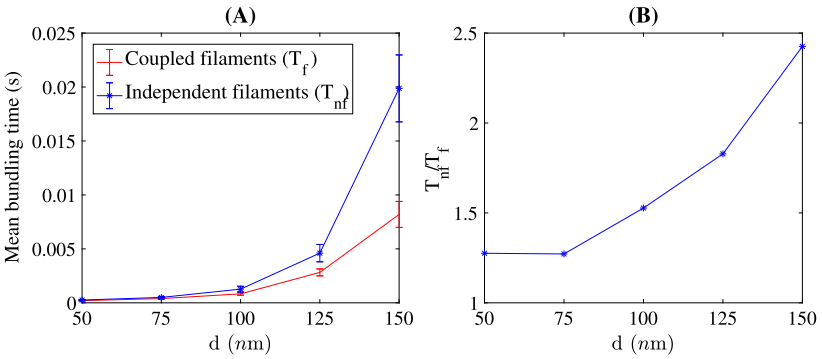

Fig. 7. [A] Mean bundling time versus the base distance d. [B] Accelerated bundling ratio T_{nf}/T_f of no-fluid (no hydrodynamic interactions between two fluids) and fluid (which includes hydrodynamics) as a function of distance d.

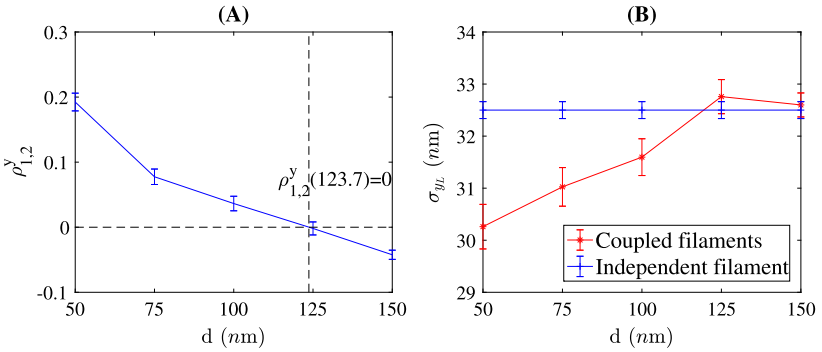

Fig. 8. [A] Correlation between the free ends of the 2 filaments. [B] Standard deviation $\sigma_{y,L}$ versus base.

We then varied the base distance d, and tested the average bundling time in our full hydrodynamic fluid simulation, T_{f}, as well as the no-fluid simulation, T_{nf}, to study the influence of the fluid. As shown in Fig. 7A, the average bundling time increases as d increases. In Fig. 7B, we plot the accelerated bundling ratio T_{nf}/T_f, which is the mean bundling time for 2 independent filaments relative to the mean bundling time for 2 coupled filaments in a fluid.

6.2. Ergodic explanation for accelerated bundling

We seek a heuristic explanation for this acceleration in bundling and why it increases, in relative terms, with increasing separation distance. There are two major hydrodynamic effects that influence the average bundling time. The first is that low-order (large wavelength) modes of thermal fluctuation cause the two filaments to move together along the same direction. This will increase the mean bundling time T_{f}. The second effect makes both filaments bend more, i.e., further from their equilibrium configurations. We can restate this in terms of the co-variance between the two filaments' y deviations,

$$\rho^{y}_{1,2} = \frac{\mathrm{cov}(\Delta y_{1,R}, \Delta y_{2,R})}{\sigma_{\Delta y_{1,R}} \sigma_{\Delta y_{2,R}}}, \tag{67}$$

where $\Delta y_{i,R}$ $(i = 1, 2)$ is the displacement of one free end with respect to its initial equilibrium position, and $\sigma_{\Delta y_{i,R}}$ is the corresponding standard deviation. As T_{nf}/T_f increases with d, $\rho^{y}_{1,2}$ decrease with d. In Fig. 8B, we plot $\sigma_{y,L}$, the standard deviation of the free ends along the y direction, versus d, the base distance. We find that this increases with d. Thus, the first effect acts to increase the correlation coefficient $\rho^{y}_{1,2}$, while the second effect acts to reduce $\rho^{y}_{1,2}$.

In the absence of hydrodynamic interactions, the covariance between filaments is zero. From our hydrodynamic-free simulations, we also know the variance is $\Delta_y = 3.25 \times 10^{-8}$ m for the free end of one single filament in a fluid. We therefore wondered if the change in bundling times could be due to the introduction of nonzero covariance and small change in variance. Approximately, $\Delta y_{1,R}(t)$ and $\Delta y_{2,R}(t)$ both appear to obey normal distributions. The joint distribution function for $\Delta y_{1,R}$ and $\Delta y_{2,R}$ is therefore approximately

$$f(\Delta y_{1,R}, \Delta y_{2,R}) = \frac{1}{2\pi\sigma^2\sqrt{1-\rho^2}} \exp\left(-\frac{1}{2(1-\rho^2)\sigma^2}\left[{\Delta y_{1,R}}^2 + {\Delta y_{2,R}}^2 - 2\rho \Delta y_{1,R}\Delta y_{2,R}\right]\right),$$

and the same for $\Delta z_{1,R}$ and $\Delta z_{2,R}$.

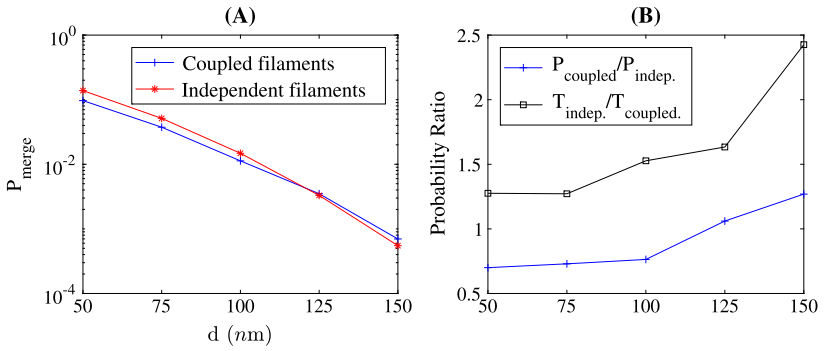

Fig. 9. [A] Probability of bundling due to sampling points. [B] Acceleration rate.

We generate 10^{10} independent sample points from this distribution, i.e., 10^{10} values for each of $\Delta y_{1,R}$, $\Delta y_{2,R}$. Note that this generates a sample of filament configurations, but no temporal dynamics. Therefore, we cannot compute bundling times, but we can compute bundling probabilities, defined as the probability that the two filament tips are within 10 nm of each other. These probabilities are shown in Fig. 9A. In Fig. 9B, we plot the accelerating rate which is the ratio between the probability of the two cases. This produces a trend of acceleration that agrees with the direct simulation results shown in Fig. 7 (but is shifted downwards).

7. Discussion

The study of hydrodynamic interactions between cytoskeletal filaments, and other cell-biological phenomena, requires a computational method that combines fluid-structure interactions with thermal fluctuations, accessing dynamics on the micron length-scale and seconds time-scale. We present such a computational scheme here. The development of this method required us to exploit several different techniques. First, we derive a large-timestep stochastic formulation in which the fluctuation sizes are damped, following previous work [16,17], allowing timesteps larger than the inertial timescale. Second, we exploit the linearity of Stokes flow and separate the fluid's velocity field into two parts, one of which is solved using the immersed boundary method, which readily handles thermal fluctuations, and the other is solved using a regularized Stokeslet method, allowing us to model a filament of finite thickness without an exceedingly small spatial discretization. Third and finally, we use multiple timesteps, with an implicit Euler scheme on the inner timestep where we impose deterministic forces. This is done to overcome the severe timestep stability criterion that arises due to bending resistance of the filament.

This method has several limitations. Accuracy is lost for larger outer timesteps (Fig. 3). In Section 5.2.1 we argue that, as the timestep grows, we lose accuracy in higher modes of deformation first, therefore we are able to match coarse filament behavior while still being computationally efficient. Nonetheless, we are able to reproduce theoretical estimates for thermal-fluctuation-driven behavior. We note that this is not possible in two-dimensional approximations of stochastic fluid dynamics, where there are issues with scaling the thermal energies [22]. (This is similar to the importance of dimensionality in single-particle Brownian motion, in which 2D and 3D behavior are qualitatively different.)

Alternative methods for simulating polymers have been developed using Stokeslets, e.g., reviewed in [38]. These studies are applied to filaments that are flexible in the thermodynamic sense, meaning their length is many times their persistence length. As F-actin filaments we study are shorter than their persistence length, the interplay between enthalpic bending and entropic exploration of angles is different from more flexible polymers like DNA. There have also been studies of short filaments using bead-spring models with hydrodynamic interaction terms, e.g., [39]. Our method is distinct in that the full flow field is computed at every timestep, something that may be informative for certain scientific questions, e.g., the role of flow on soluble particles.

Our results add to a growing body of research (e.g., [4]) suggesting that hydrodynamic interactions may be significant for biopolymer interactions in cells. Specifically, we studied the role of hydrodynamics in F-actin bundling. The detailed, mechanistic study of actin bundling is of continuing value [40–42]. Recent studies highlighted the role several different bundling proteins in different scenarios, such as fascins, which are implicated in bundling F-actin to form the "invadopodia" that power cancer cell metastasis [43,44], and L-plastin that bundles F-actin to enable the immune activity of lymphocytes [45,46].

This work will enable us to study how hydrodynamics influences other F-actin dynamic processes. For example, one of the primary F-actin nucleation mechanisms employs Arp2/3 to create new filaments branching off existing ones at a precisely controlled 70° angle [23]. Recent evidence suggests that, in some circumstances, these branched F-actin networks can transform into bundled F-actin arrays [47], raising the question of how two semi-flexible filaments, joined at a rigid clamp of 70°, can fluctuate into sufficient proximity for bundling. Another question relates to the action of F-actin interacting with a membrane. Here, F-actin can grow by addition of new monomers, but only upon thermally fluctuating away from the membrane in a phenomenon termed the Brownian ratchet [13]. In vivo, many such F-actin filaments appose a single

membrane to generate large-scale (nanonewton) forces on the membrane. The additivity of this ensemble of filaments is observed to be non-linear [48,49], raising the question of whether hydrodynamic interactions could be playing a major role here. The present work opens up this important regime of spatial, temporal and energy scales for future simulation.

Acknowledgements

K.L. and J.A. are partially supported by NSF grant CAREER DMS-1454739 (to J.A). K.L. and J.L. are partially supported by NSF grant DMS-0915128 (to J.L.). J.L. is supported by NSF grant DMS-1129008. In addition, J.A., and J. L. also thank partial support from the National Institutes of Health through grant P50GM76516, NSF grant DMS 1763272 and a grant from the Simons Foundation (594598, QN).

References

[1] B. Guirao, et al., Coupling between hydrodynamic forces and planar cell polarity orients mammalian motile cilia, Nat. Cell Biol. 12 (4) (2010) 341–350.
[2] K. Manakova, H. Yan, J. Lowengrub, J. Allard, Cell surface mechanochemistry and the determinants of bleb formation, healing, and travel velocity, Biophys. J. 110 (2016) 1636–1647.
[3] J.-Y. Tinevez, U. Schulze, G. Salbreux, J. Roensch, J.-F. Joanny, E. Paluch, Role of cortical tension in bleb growth, Proc. Natl. Acad. Sci. 106 (44) (2009) 18581–18586.
[4] E. Nazockdast, et al., Cytoplasmic flows as signatures for the mechanics of mitotic positioning, arXiv:1511.02508 [physics.bio-ph], 2017, pp. 1–32.
[5] K. Yi, J. Unruh, M. Deng, B. Slaughter, B. Rubinstein, R. Li, Dynamic maintenance of asymmetric meiotic spindle position through Arp2/3-complex-driven cytoplasmic streaming in mouse oocytes, Nat. Cell Biol. 13 (10) (2011) 1252–1258.
[6] M. Bergert, A. Erzberger, R. Desai, I. Aspalter, A. Oates, G. Charras, G. Salbreux, E. Paluch, Force transmission during adhesion-independent migration, Nat. Cell Biol. 17 (4) (2015) 524–529.
[7] A. Siryaporn, M. Kim, Y. Shen, H. Stone, Z. Gitai, Colonization, competition, and dispersal of pathogens in fluid flow networks, Curr. Biol. 25 (9) (2015) 1201–1207.
[8] J. Lowengrub, J. Allard, S. Aland, Numerical simulation of endocytosis: viscous flow driven by membranes with non-uniformly distributed curvature-inducing molecules, J. Comput. Phys. 309 (2016) 112–128.
[9] A. Carlson, L. Mahadevan, Elastohydrodynamics and kinetics of protein patterning in the immunological synapse, PLoS Comput. Biol. 11 (12) (2015) e1004481-16.
[10] C. Peskin, The immersed boundary method, Acta Numer. (2002) 479–517.
[11] W. Strychalski, C. Copos, O. Lewis, R. Guy, A poroelastic immersed boundary method with applications to cell biology, J. Comput. Phys. 282 (C) (2015) 77–97.
[12] T. Shinar, M. Mana, F. Piano, M. Shelley, A model of cytoplasmically driven microtubule-based motion in the single-celled Caenorhabditis elegans embryo, Proc. Natl. Acad. Sci. 108 (26) (2011) 10508–10513.
[13] A. Mogilner, G. Oster, Cell motility driven by actin polymerization, Biophys. J. 71 (6) (1996) 3030–3045.
[14] L. Yang, D. Sept, A. Carlsson, Energetics and dynamics of constrained actin filament bundling, Biophys. J. 90 (12) (2006) 4295–4304.
[15] C.-H. Wu, T. Fai, P. Atzberger, C. Peskin, Computational methods in science and engineering simulation of osmotic swelling by the stochastic immersed boundary method, SIAM J. Sci. Comput. 37 (4) (2015) B660–B688.
[16] P.J. Atzberger, A stochastic immersed boundary method for fluid-structure dynamics at microscopic length scales, J. Comput. Phys. 224 (2007) 1255–1292.
[17] P. Atzberger, Stochastic Eulerian Lagrangian methods for fluid structure interactions with thermal fluctuations, J. Comput. Phys. 230 (2011) 2821–2837.
[18] P. Kramer, C. Peskin, P. Atzberger, On the foundations of the stochastic immersed boundary method, Comput. Methods Appl. Mech. Eng. 197 (2008) 2232–2249.
[19] J. Sigurdsson, F. Brown, P. Atzberger, Hybrid continuum-particle method for fluctuating lipid bilayer membranes with diffusing protein inclusions, J. Comput. Phys. 252 (2013) 65–85.
[20] J.M. Ortiz de Zarate, J. Sengers, Hydrodynamic Fluctuations in Fluids and Fluid Mixtures, Elsevier Press, 2006.
[21] I. Cialenco, N. Glatt-Holtz, Parameter estimation for the stochastically perturbed Navier–Stokes equations, Stoch. Process. Appl. 121 (2011) 701–724.
[22] K. Liu, C. Hamilton, J. Allard, J. Lowengrub, S. Li, Wrinkling dynamics of fluctuating vesicles in time-dependent viscous flow, Soft Matter 12 (26) (2016) 5663–5675.
[23] T. Pollard, J. Cooper, Actin, a central player in cell shape and movement, Science 326 (2009) 1208–1212.
[24] Y. Kim, M.-C. Lai, Simulating the dynamics of inextensible vesicles by the penalty immersed boundary method, J. Comput. Phys. 229 (2010) 4840–4853.
[25] B.K. Oksendal, Stochastic Differential Equations: An Introduction with Applications, Springer, Berlin, 2003.
[26] R. Cortez, The method of regularized Stokeslets, SIAM J. Sci. Comput. 23 (2001) 1204–1225.
[27] R. Cortez, L. Fauc, A. Medovikovcm, The method of regularized Stokeslets in three dimensions: analysis, validation, and application to helical swimming, Phys. Fluids 17 (2005) 031504.
[28] Elizabeth L. Bouzarth, Anita T. Layton, Yuan-Nan Young, Modeling a semi-flexible filament in cellular Stokes flow using regularized Stokeslets, Int. J. Numer. Methods Biomed. Eng. 27 (12) (2011) 2021–2034.
[29] T. Odjik, Stiff chains and filaments under tension, Macromolecules 28 (1995) 7016–7018.
[30] C.G. Broyden, A class of methods for solving nonlinear simultaneous equations, Math. Comput. 19 (92) (1965) 577–593.
[31] Klement, On using quasi-Newton algorithms of the Broyden class for model-to-test correlation, J. Aerosp. Technol. Manag. 6 (4) (2014) 407–414.
[32] S.K. Veerapaneni, D. Gueyffier, D. Zorin, A boundary integral method for simulating the dynamics of inextensible vesicles suspended in a viscous fluid in 2D, J. Comput. Phys. 228 (2009) 2334–2353.
[33] M. Kraus, W. Wintz, U. Seifert, R. Lipowsky, Fluid vesicles in shear flow, Phys. Rev. Lett. (1996).
[34] W. Luo, C. Yu, Z. Lieu, J. Allard, A. Mogilner, M. Sheetz, A. Bershadsky, Analysis of the local organization and dynamics of cellular actin networks, J. Cell Biol. 202 (2013) 1057–1073.
[35] P.E. Kloeden, E. Platen, Numerical Solution of Stochastic Differential Equations, Springer, 1992.
[36] K. Burrage, T. Tian, The composite Euler method for stiff stochastic differential equations, J. Comput. Appl. Math. (2001).
[37] R. Wollman, E.N. Cytrynbaum, J.T. Jones, T. Meyer, J.M. Scholey, A. Mogilner, Efficient chromosome capture requires a bias in the “search-and-capture” process during mitotic-spindle assembly, Curr. Biol. 15 (9) (2005) 828–832.
[38] M.D. Graham, Fluid dynamics of dissolved polymer molecules in confined geometries, Annu. Rev. Fluid Mech. 43 (2011) 273–298.
[39] F. Meshkati, H.C. Fu, Modeling rigid magnetically rotated microswimmers: rotation axes, bistability, and controllability, Phys. Rev. E 90 (2014) 063006.
[40] A. Michelot, D. Drubin, Building distinct actin filament networks review in a common cytoplasm, Curr. Biol. 21 (14) (2011) R560–R569.

[41] P. Kraikivski, B. Slepchenko, I. Novak, Actin bundling: initiation mechanisms and kinetics, Phys. Rev. Lett. 101 (12) (2008) 128102.
[42] Y. Ideses, Y. Brill-Karniely, L. Haviv, A. Ben-Shaul, A. Bernheim-Groswasser, Arp2/3 branched actin network mediates filopodia-like bundles formation in vitro, PLoS ONE 3 (2008) e3297–e3299.
[43] A. Li, J. Dawson, M. Forero-Vargas, H. Spence, X. Yu, I. Konig, K. Anderson, L. Machesky, The actin-bundling protein fascin stabilizes actin in invadopodia and potentiates protrusive invasion, Curr. Biol. 20 (4) (2010) 339–345.
[44] A. Nürnberg, T. Kitzing, R. Grosse, Nucleating actin for invasion, Nat. Rev. Cancer 11 (3) (2011) 177–187.
[45] S.C. Morley, The actin-bundling protein L-plastin supports T-cell motility and activation, Immunol. Rev. 256 (1) (2013) 48–62.
[46] X. Xu, et al., Mst1 kinase regulates the actin-bundling protein L-plastin to promote T cell migration, J. Immunol. 197 (5) (2016) 1683–1691.
[47] Y. Brill-Karniely, Y. Ideses, A. Bernheim-Groswasser, A. Ben-Shaul, From branched networks of actin filaments to bundles, ChemPhysChem 10 (16) (2009) 2818–2827.
[48] J. Zhu, A. Mogilner, Mesoscopic model of actin-based propulsion, PLoS Comput. Biol. 8 (11) (2012) e1002764.
[49] E. Barnhart, J. Allard, S. Lou, J. Theriot, A. Mogilner, Adhesion-dependent wave generation in crawling cells, Curr. Biol. 27 (1) (2017) 27–38.